Journal of Power Sources 297 (2015) 540–550

Contents lists available at ScienceDirect

Journal of Power Sources

journal homepage: www.elsevier.com/locate/jpowsour

Modeling the evolution of lithium-ion particle contact distributions using a fabric tensor approach

A.J. Stershic [a, *], S. Simunovic [b], J. Nanda [b]

[a] Department of Civil and Environmental Engineering, Duke University, Durham, NC 27708, USA
[b] Oak Ridge National Laboratory, One Bethel Valley Road, Oak Ridge, TN 37831, USA

HIGHLIGHTS

- We examine the microstructure of lithium nickel manganese cobalt oxide cathodes.
- We search for active material contacts in tomography by geometric approximations.
- Fabric tensors can be used to model directional contact distribution.
- DEM models built from particle size distribution do not reflect experimental data.

GRAPHICAL ABSTRACT

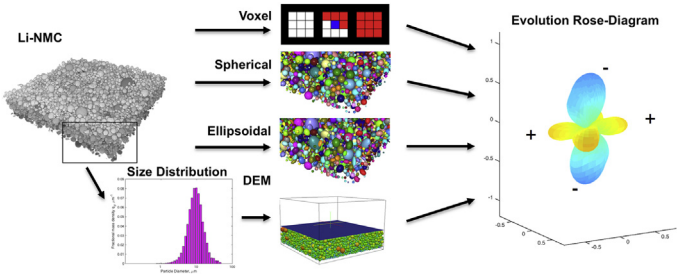

ARTICLE INFO

Article history:
Received 7 April 2015
Received in revised form
24 July 2015
Accepted 28 July 2015
Available online xxx

Keywords:
Fabric tensor
Lithium-ion battery
NMC
DEM

ABSTRACT

Electrode microstructure and processing can strongly influence lithium-ion battery performance such as capacity retention, power, and rate. Battery electrodes are multi-phase composite structures wherein conductive diluents and binder bond active material to a current collector. The structure and response of this composite network during repeated electrochemical cycling directly affects battery performance characteristics. We propose the fabric tensor formalism for describing the structure and evolution of the electrode microstructure. Fabric tensors are directional measures of particulate assemblies based on inter-particle connectivity, relating to the structural and transport properties of the electrode. Fabric tensor analysis is applied to experimental data-sets for positive electrode made of lithium nickel manganese cobalt oxide, captured by X-ray tomography for several compositions and consolidation pressures. We show that fabric tensors capture the evolution of inter-particle contact distribution and are therefore good measures for the internal state of and electronic transport within the electrode. The fabric tensor analysis is also applied to Discrete Element Method (DEM) simulations of electrode microstructures using spherical particles with size distributions from the tomography. These results do not follow the experimental trends, which indicates that the particle size distribution alone is not a sufficient measure for the electrode microstructures in DEM simulations.

1. Introduction

Lithium-ion batteries are currently a storage technology of choice for applications ranging from automotive to consumer electronics due to their high energy density, performance, and versatility [17]. An increasing demand for high-capacity, high-

* Corresponding author.
E-mail addresses: andrew.stershic@duke.edu (A.J. Stershic), simunovics@ornl.gov (S. Simunovic), nandaj@ornl.gov (J. Nanda).

http://dx.doi.org/10.1016/j.jpowsour.2015.07.088
0378-7753/

power batteries for hybrid and electric vehicles [46] and grid energy storage [22] has resulted in the development of new active materials for Li-ion electrodes and battery chemistries [30,51]. The microstructure and processing of the Li-ion battery electrodes has a strong influence on their performance and life [44,6,48]. The electrode microstructure is set at the electrode manufacturing step and evolves during battery operation usually causing deterioration of the battery performance. As the demands for Li-ion technology grow in terms of delivering high energy and power, consideration must be given to the transport, mechanical, and thermal behavior of the electrode microstructures in order to optimize storage, useful life, and thermal safety [3].

Li-ion positive electrodes are multi-phase materials comprising both active and inactive phases. The active phase is usually in the form of crystalline or semi-crystalline powder and accounts for about 90% of the total mass of the electrode. The remaining mass is partitioned between the two inactive materials: binder and conductive agent. The positive active materials for Li-ion batteries are typically lithiated transition-metal oxides such as $LiNi_{1/3}Mn_{1/3}Co_{1/3}O_2$ (NMC), $LiCoO_2$, $LiNi_{0.8}Co_{0.15}Al_{0.05}O_2$, $LiMn_2O_4$, $LiFePO_4$, and $LiMn_{1.5}Ni_{0.5}O_4$ [17]. Carbon black is used as a conducting additive for enhancing the electrical contact between particles. Polyvinylidene fluoride (PVDF) is a common binder that holds the active particles together and onto the current collector. The interplay between the three electrode constituents is more complex than their primary roles suggest, especially under processing conditions where mechanical effects such as calendaring can induce significant changes in the electrode microstructure [52]. As an example, too little binder results in a low connectivity between the active particles, impeding electronic conductivity and electrochemical performance [52]. Too much binder makes the overall electrode more insulating. An electronically-conducting additive may boost local electronic conductivity but may constrict the overall ionic transport at electrode level.

The active electrode material, binder, and conductive agent form a porous solid skeleton. The overall porosity can range from 20 to 30% which allows the liquid electrolyte to access the active material [17]. Currently, the main parameters for electrode microstructure characterization are active particle average size, size distribution, and electrode porosity [6,7]. These parameters can be related to battery performance, especially in the post-production stage [42,52], but they often require empirical correlations and are insensitive to many types of changes in the microstructure that occur at the electrode level [23,13]. For example, Ebner et al. [12] shows that positive electrode assemblies forming an anisotropic structure suffer increased tortuosity perpendicular to current collection, which can negatively impact power density and battery performance. This shows that the particle size distribution and porosity alone are insufficient to describe the transport mechanisms in the electrode. Another example is adhesion loss between the binder/conductive agent and active particles; this may reduce the electrical conductivity of the assembly but changes neither the active particle size distribution nor the overall porosity. Similarly, particle rearrangement does not change the size distribution, although it may change the electrode porosity.

One method to simulate and analyze electrode particulate microstructures is the Discrete Element Method (DEM). Originally developed by Cundall and Strack [8] for modeling granular mechanics, it has been recently applied to various aspects of electrode microstructures [6,7]. However, these models must be upscaled to the continuum scale in order to be of a practical use, and methods of scaling are yet to be developed for electrode structures.

The transport properties in the electrode are strongly influenced by the connectivity of the active material particles and the connectivity of the interstitial space. The electrode microstructure and transport domains are similar to those of the saturated granular materials and bonded porous aggregates [37], so our idea is that some of the descriptive and analytical tools [20,36] of the latter can be applied to electrodes. In fact, the electrical conductivity and percolation are often used as analogs for modeling strength and material breakdown [29]. In granular media, the mechanical connectivity, force networks, and transport are described using Fabric Tensor (FT) formulations. FTs are well-established, non-local directional measures of internal connectivity and structure of granular media and solids. They are also extensively used in the field of damage mechanics [45,47,37] to describe the deterioration of material due to cracks and the reduction in the connectivity and force transport pathways. They provide granular and damage mechanics with a measurable and clear physical interpretation of microstructure effects and correlate to macroscopic properties such as skeleton stress tensors and stiffness tensors.

In the remainder of the paper, we investigate the use of FTs to describe microstructure of battery electrodes. We focus on the directionality of the active material contact network and structural mechanics aspects of the material as they are the most closely related to the disciplines where FT formulations have been extensively used. Following the same ideas for thermal, charge, and species transport gives us exciting new possibilities for creating unified framework for modeling battery performance based on the electrode microstructures. We seek to show that FTs are an appropriate measure of particle contact for lithium-ion positive electrode microstructures, and further, how the particle assembly responds to processing steps such as calendaring pressure. This will provide a metric for evaluating and standardizing the microstructural evolution under such conditions. The concept is illustrated on the experimental scanned microstructure of NMC electrodes and their DEM simulated models. By combining experimental imagery and DEM simulations, the FT framework can be employed to build constitutive models of the electrode microstructure, as has been done with granular media, which will be subject of subsequent publications.

2. Experimental data

Tomographic imagery used in this study was collected by Ebner et al. [13] using the synchrotron radiation X-ray tomographic microscopy (SRXTM) technique, yielding an imagery set which can be assembled to form a three-dimensional image of the cathode microstructure. Tomographic measurement was performed on electrodes that were earlier calendared at pressures of approximately 300, 600, and 2000 bar (30, 60, and 200 MPa, respectively) as well as uncalendared samples (0 bar, 0 MPa). The sample preparation for tomography involves placing electrodes in cylindrical molds (15 mm diameter), immersing them in epoxy resin, and heating them for 24 h at 55 °C under vacuum [13]. Cylindrical samples 0.7 mm in width are then milled using a lathe [13].

The Laboratory of Nanoelectronics at the Eidgenössische Technische Hochschule Zürich (ETHZ) performed the step of particle identification using the watershed algorithm for particle segmentation, detailed for granular contact problems by Saadatfar [40]. The database is hosted by ETHZ Library and is publicly available [21]. It includes the raw imagery files, time-series data of charging cycles, and a tabulated description of the identified particles. The imagery slices are approximately 330 μm × 330μm square with voxels that measure 370 nm × 370nm × 370nm.

The materials used to make the cathode composite were NMC compound from 3M, Super C65 carbon black from TIMCAL Ltd., and Kynar 761 binder (polyvinylidene fluoride) from Arkema [13,6]. Chung et al. [6] notes that the NMC compound was selected due to the high sphericity of the particles, which are distributed log-

normally in size with a mean radius of $\bar{r} = 6\mu$m and a polydispersity of $\delta = 0.6\bar{r}$. The cathode compositions tested are of the mass fraction ratios of NMC to carbon black to binder described in Table 1.

3. Fabric tensor formalism

There are several commonly-used scalar and tensorial methods of describing the relative positions of particles in an assembly or bonded aggregate [37]. Scalar methods include void fraction, porosity, and coordination number [37]. These metrics characterize the quantity of inter-particle contacts or their density, but do not characterize their directionality. Given our interest in contacting particles, coordination number is the most appropriate of the scalar quantities. Coordination number is a scalar measure of contact, indicating the average number of contacts a particle has [37]. This scalar estimate is correlated to particle packing metrics like void ratio [37]. The average coordination number of the assembly can be calculated as $z = n_c/n_p$ where n_c is the number of contacts and n_p is the number of particles [37]. This is a straightforward metric to analyze the quantity of inter-particle contacts, making it a common metric for microstructural analysis [50]; but in contrast to FTs, it contains no directional information, limiting its ability to describe complex and anisotropic particle assemblies.

FT is a numerical approximation to a directional data-set in a multidimensional space, pioneered by Satake [41] and Kanatani [18]. FT analysis is an established technique in the granular mechanics community with applications to modeling evolution of solid skeleton configuration and for developing homogenized material properties for anisotropically-damaged materials [38]. The tensors can be constructed from particle contact vectors, branch vectors, orientation vectors, and combinations thereof [37]. These tensors are able to capture anisotropic, or directionally-dependent, characteristics of a particle assembly by preserving directionality in a multi-dimensional structure. The contact vectors used to build the FT in this study are the centroid vectors (branch vector) and the contact patch normals (see illustration in Fig. 1).

Before FTs can be calculated, the list of inter-particle contact vectors between all particles in the assembly is required. We use three approximation techniques for contact vector calculations, each using a different methodology to derive this list for each of the experimental data-sets. The most direct approach is to use the three dimensional X-ray tomography with labeled particles and check for contact of differently labeled voxels. While straightforward to implement, using the voxels to directly derive a contact vector depends heavily on the resolution of the tomography. For each voxel, contact is only possible in 26 discrete directions, limiting the ability of the contact vector to accurately represent what may be a smooth surface in reality. These 26 directions represent contact vectors between one voxel and any of those surrounding it in a $3 \times 3 \times 3$ voxel cube (6 directly adjacent and 20 diagonal), all having a distance of one voxel in the infinity norm, L_∞. To mitigate the voxel discretization effect, we consider both branch vectors and averaged contact patch normals for contact vectors.

The two remaining methods for contact vector calculation are based on geometric approximations of the active particles: spherical and ellipsoidal. These alternatives yield vectors that do not directly depend on the imagery resolution. A comparison between raw tomography, polygonally-meshed particles, spherical approximations, and ellipsoidal approximations is depicted in Fig. 2. The details of the methods for contact vector calculations are given in Appendix A. Once the contact vectors are available, the FTs are straightforward to calculate [47] and have been implemented in several software libraries. Here we use the software MMTensor [27] in MATLAB.

Table 1
Cathode matrix composition.

NMC (%)	Carbon black (%)	PVDF binder (%)
90	5	5
92	4	4
94	3	3
96	2	2

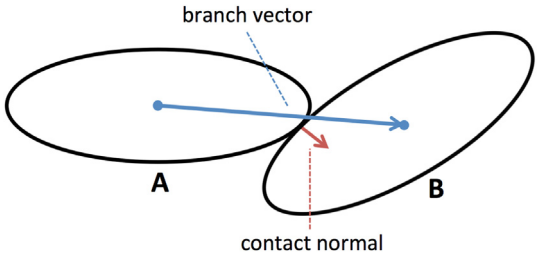

Fig. 1. Illustration of ellipses in contact, showing branch vector from centroid to centroid (blue) and contact normal vector (red). (For interpretation of the references to color in this figure legend, the reader is referred to the web version of this article.)

The primary comparison technique used in this study to evaluate the evolution of NMC active particle contact direction during the calendaring process is comparison of FTs. The expected benefit of using tensor representations of contact distributions is clear: a more realistic model of particle connectivity as conditions change within the battery. The organizational state of particle assemblies is dependent on its deformation history; applying the FT will allow for better characterization of the cathode assembly [37].

Three kinds of FTs have been developed to approximate an experimental directional data-set $\vec{n}$: first, **N**, a weighted moment tensor; second, **F**, a least-squares-based tensor ("fabric tensor"); and third, **D**, an orthogonal decomposition of the second ("deviatoric tensor") [18,37]. FTs of the third kind, **D**, of any order k can be derived from their second kind counterparts, **F**, by $\mathbf{D}^{(k)} = \mathbf{F}^{(k)} - \delta^{(2)}\mathbf{F}^{(k-2)}$ [37]. FTs representing directional distributions of unit vectors are symmetric about the origin, $f(\vec{n}) = f(-\vec{n})$ and sum to one on a unit surface: $\int_\Gamma f(\vec{n})d\Gamma = 1$ (Γ is a unit circle in 2-D or unit sphere 3-D) [37]. In this work, the FTs are generally referred to as **N**, **F**, and **D** with order given as an exponent (ex. $\mathbf{F}^{(k)}$). FTs and the contact vectors can be equivalently represented in indicial notation (e.g. $F_{ij}^{(2)}, D_{ijkl}^{(4)}, n_i$), in which summation of repeated indices is implied (ex. "$D_{ij}^{(2)} n_i n_j$" $= \sum_{i=1}^{length(\vec{n})} \sum_{j=1}^{length(\vec{n})} D_{ij}^{(2)} n_i n_j$).

FTs of the second and third kind can be used to build a k-th order approximation, $f^{(k)}(\vec{n})$, of the true directional distribution of the directional data-set $\widehat{f}(\vec{n})$ by serving as coefficients for a polynomial expansion [18,37]:

$$\begin{aligned}\widehat{f}(\vec{n}) \approx f^{(k)}(\vec{n}) &= \frac{1}{4\pi}\left(F_{i_1\ldots i_k}^{(k)} n_{i_1}\ldots n_{i_k}\right) \\ &= \frac{1}{4\pi}\left(D^{(0)} + D_{ij}^{(2)} n_i n_j + D_{ijkl}^{(4)} n_i n_j n_k n_l + \ldots \right. \\ &\quad \left. + D_{i_1\ldots i_k}^{(k)} n_{i_1}\ldots n_{i_k}\right) \end{aligned} \quad (1)$$

The zeroth-, second-, and fourth-rank (or order) FTs of the first, second, and third kind can be computed for a data-set consisting of N vectors, as illustrated in Eqs. (2)–(4) [47,18]. In this analysis, we are interested in only the direction of the contact vectors, so the unit vectors of the contact vectors are used in the construction of

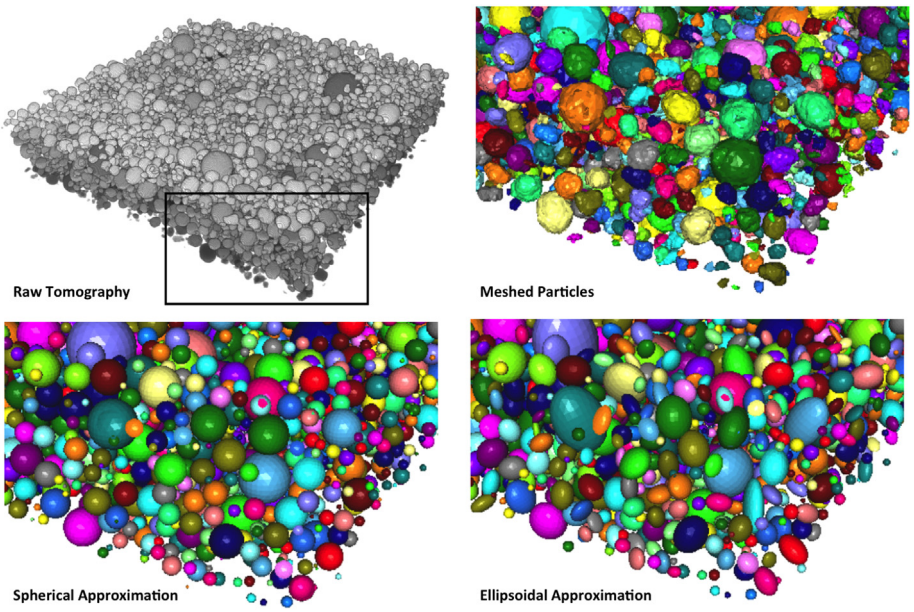

Fig. 2. NMC 92% wt. 0 bar sample: (top-left) stacked raw tomography, showing zoom box; (top-right) meshed particles, zoomed; (bottom-left) spherical approximations to particles, zoomed; (bottom-right) ellipsoidal approximations to particles, zoomed. Note: colors indicate unique particles but do not correspond. (For interpretation of the references to color in this figure legend, the reader is referred to the web version of this article.)

FTs. Cambou et al. [37] indicates that second-rank tensors are often insufficient to characterize the directional distribution of contacts in granular assemblies with complex contact histories, encouraging the use of fourth-rank tensors.

$$N^{(0)} = \frac{1}{N}\sum_{\alpha=1}^{N} 1 = 1 \quad N_{ij}^{(2)} = \frac{1}{N}\sum_{\alpha=1}^{N} n_i^\alpha n_j^\alpha \quad N_{ijkl}^{(4)} = \frac{1}{N}\sum_{\alpha=1}^{N} n_i^\alpha n_j^\alpha n_k^\alpha n_l^\alpha \tag{2}$$

$$F^{(0)} = N^{(0)} = 1 \quad F_{ij}^{(2)} = \frac{15}{2}\left(N_{ij}^{(2)} - \frac{1}{5}\delta_{ij}\right)$$
$$F_{ijkl}^{(4)} = \frac{315}{8}\left(N_{ij}^{(4)} - \frac{2}{3}\delta_{ij}N_{kl}^{(2)} + \frac{1}{21}\delta_{ij}\delta_{kl}\right) \tag{3}$$

$$D^{(0)} = N^{(0)} = 1 \quad D_{ij}^{(2)} = \frac{15}{2}\left(N_{ij}^{(2)} - \frac{1}{3}\delta_{ij}\right)$$
$$D_{ijkl}^{(4)} = \frac{315}{8}\left(N_{ij}^{(4)} - \frac{6}{7}\delta_{ij}N_{kl}^{(2)} + \frac{3}{35}\delta_{ij}\delta_{kl}\right) \tag{4}$$

FTs can be visually represented by a rose diagram, a polar plot that indicates the frequency of distribution as a radius for a given contact direction. An example of the rose diagram for the second-rank FT of the first kind, $\mathbf{N}^{(2)}$, is given in Fig. 3 (left) for the 90% wt. NMC, 0 bar data-set with the voxel contact vector approximation. This shape is ellipsoidal and nearly spherical, which indicates that the contact distribution is nearly uniform.

The corresponding fourth-rank FT of the first kind, $\mathbf{N}^{(4)}$, for this data-set is shown in Fig. 3 (center). The dimpled top and bottom faces and a slightly more square body illustrates the added geometrical complexity of the fourth-rank tensor; this represents that the contact distribution has relatively more contacts in the diagonal directions and fewer in the vertical direction. A comparison of the second- and fourth-rank FTs of the second kind ($\mathbf{F}^{(2)}$ vs. $\mathbf{F}^{(4)}$) for the 90% wt. NMC, 0 bar data-set is given in Fig. 3 (right). This shows the two FTs overlaid, highlighting the simpler geometric shape of the second-rank tensor and the knobbier shape of the fourth-rank tensor.

When comparing contact distribution between two different calendaring pressures, we compute the difference between the density distributions that the FTs represent: $\Delta f^{(a,b)} = f(\mathbf{F}_{2000}^{(b)}) - f(\mathbf{F}_{0}^{(a)})$. The differences indicate how the contact distribution shifts with increasing pressure. Because FTs are normalized by the number of contacts to show the distribution, their zeroth-rank approximation (interpreted as an average) is a sphere of constant radius: $f^{(0)} = \int_\Gamma f(\vec{n})d\Gamma / \int_\Gamma d\Gamma = 1/4\pi$. The density differences (Δf), then, have an "average" of zero, but are composed of positive and negative zones, where the compared tensors differ. In this way, we can compare the FTs of two different data-sets to see how the contact distribution of the particles evolves (see illustration in Fig. 4).

When rose diagrams of the density differences have positive petals (yellow to orange to red in Fig. 4), this indicates that with increasing pressure, contacts tend to increase in frequency in the direction of the petal. Likewise, negative petals (green to teal to blue in Fig. 4) indicate that contacts tend to decrease in frequency as pressure increases. An example of the FT analysis is given in Fig. 4. Here the fourth-order FTs of the 90% wt. NMC data-set constructed from the branch vectors of the ellipsoidal approximation are compared between the 0 bar and 2000 bar data-sets. The difference of the two tensors, indicated by the right-most plot, shows that as the pressure increases from 0 bar to 2000 bar, the contact distribution is decreasingly vertical and increasingly lateral.

In this study, we analyze the density differences between fabric tensors derived from X-ray tomography using various representations of particle geometry and contact. Specifically, we observe changes in vertical and lateral contact distribution as the calendaring pressure increases. We generated zeroth-, second- and fourth-rank FTs for each contact network approximation for all data-sets. Fourth-rank FTs of the second kind are the primary means of comparison, and tensors of the third kind are computed to test for the fitness of the approximations (see Appendix B). The results and trends are compared to simulated particle configurations using DEM with particle size distribution from the experiments.

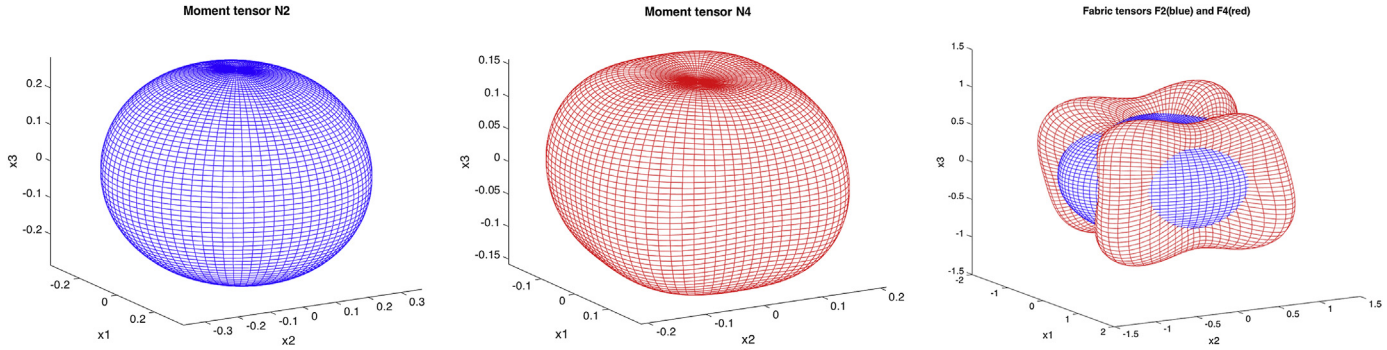

Fig. 3. 90% wt. NMC, 0 bar data-set (voxel contact vector approximation): $\mathbf{N}^{(2)}$ (left) and $\mathbf{N}^{(4)}$ (center) fabric tensor rose diagrams; (right) comparison of $\mathbf{F}^{(2)}$ (blue) and $\mathbf{F}^{(4)}$ (red) fabric tensor approximations to data-set. (For interpretation of the references to color in this figure legend, the reader is referred to the web version of this article.)

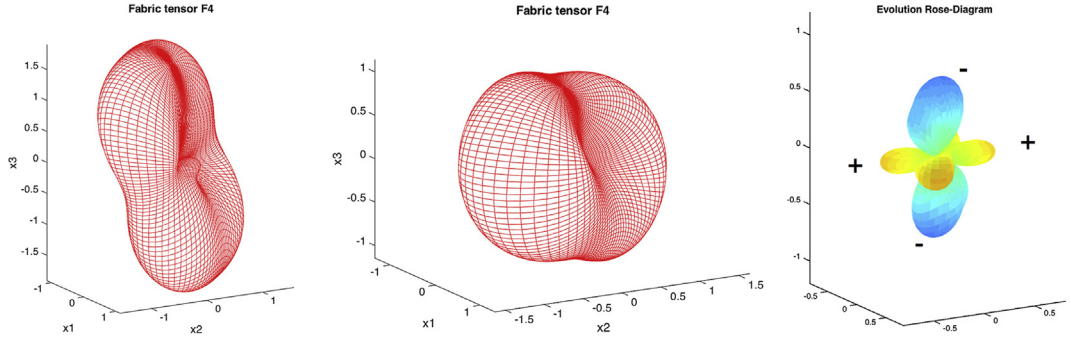

Fig. 4. Example of fabric tensor analysis (90% wt. NMC, ellipsoidal approximation, branch vector). Fabric tensor of unloaded assembly $\mathbf{F}_0^{(4)}$ (left) is subtracted from fabric tensor of loaded assembly $\mathbf{F}_{2000}^{(4)}$ (center) to produce an evolution rose-diagram (right). Yellow to orange to red areas show positive change, green to teal to blue areas show negative change. (For interpretation of the references to color in this figure legend, the reader is referred to the web version of this article.)

4. DEM simulation

In this study, we investigate FT evolution for simulated electrode microstructures. The discrete element method (DEM) is a leading model for simulating particulate and granular assemblies on a wide range of material scales, from atomistic and molecular dynamics to landslides and avalanches [36]. More recently, DEM has been applied to model electrode microstructures due to the particulate nature of the active material [6,7]. We seek to evaluate the use of DEM simulations to characterize electrode microstructure by analyzing the evolution of the contact network with the fabric tensor formalism.

The DEM simulation is used to first create a domain equivalent to the ETHZ data-sets before pressure is applied and then to compress the domain until the desired pressure is reached. In order to accomplish this task, we used LIGGGHTS, a leading open-source DEM code from DCS Computing GmbH based off the LAMMPS molecular dynamics simulator from Sandia National Laboratories [19,35].

We use the particle gradation from the ETHZ data-set (see Fig. 5) to randomly generate a set of polydisperse spherical particles that settle under gravity, packing the domain until the desired sample is created, a common approach for DEM simulation of granular media [13]; recent research has used this approach for simulation with both monodisperse (uniformly-sized) and polydisperse particles [50,6,7,31]. The Hertzian contact model with friction is used as the interaction law between the particles in the DEM simulation. This choice is not expected to have a significant impact on the NMC particle packing, as other models have shown to yield similar results for granular packing simulations [11]. Other forces such as Van der Waals, capillary, and electrostatic are assumed to be negligible in comparison, which is common for granular simulations [50]. The inclusion of Van der Waals forces has been found to be significant for the results of some micrometer-scale particle simulations [31] but for not others [11].

The boundary conditions used during packing approximate conditions in the ETHZ experiments: boundaries of aluminum on the bottom to represent the current collector, steel on the top to represent the roller, and periodic boundaries on the sides to avoid edge effects [50]. Parameters used for the DEM simulation can be found in Table 2.

Once the geometry is generated, the material properties are ascribed to the particles, and then a downward-moving plate is inserted to compress the domain. The 0 bar values are measured after the particles settle but before the plate contacts the assembly. The volume fraction of this particle packing at 0 bar is within 0.06–0.11 of the volume fraction estimates of the tomography (see Table 3), indicating that the DEM-generated packing is slightly denser than the experimental data. The plate is assigned material properties of steel to represent the roller in the calendaring process. When each of the pressure levels is attained (0 bar, 300 bar, 600 bar, 2000 bar), the list of contact vectors is assembled for FT analysis.

Desmond et al. [9] defines an index of polydispersity as being equal to the coefficient of variation of the particle size distribution, $\delta =$ std.dev./mean, in order to characterize the variation of particle sizes and predict packing fraction. The densest random close packing (RCP) of monodisperse spheres typically yields a volume fraction of about 0.64, while with perfect arrangement (face-centered-cubic or hexagonal-close-packed) it may be as high as 0.74 [5,9]. Polydisperse packings can be higher still, as smaller

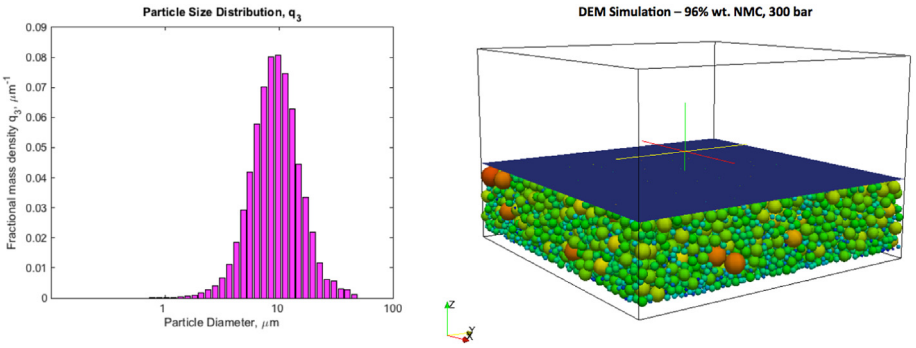

Fig. 5. (Left) Particle size distribution by diameter (fractional mass density q_3) of ETHZ data-set [21]; (right) DEM simulation of 96% wt. NMC material at 300 bar, simulation domain measures 340 μm × 340 μm × 220 μm.

Table 2
DEM simulation parameters.

Parameter	NMC	Steel	Aluminum
ρ, Density	4750 kg/m^3	7750 kg/m^3	2700 kg/m^3
E, Young's modulus	113 GPa	200 GPa	69 GPa
ν, Poisson's ratio	0.25	0.3	0.32
μ, Coefficient of friction w/NMC:	0.15	0.15	0.15
Contact Law	Hertzian	Hertzian	Hertzian

particles can fill the pores left by a dense packing of larger particles [9]. Common methods of generating these RCP assemblies are to place particles and then expand and move them to avoid overlap [9] or to pour the particles into a box [43]. Desmond et al. [9] uses the former method to propose a prediction for the volume fraction of particles (packing fraction) as a function of polydispersity (δ) and distribution skewness (S): $\Phi_{RCP} = 0.637 + 0.0658 \cdot \delta + 0.0857 \cdot S\delta^2$.

Chung et al. [6] characterizes the particle size distribution of the NMC particles in the ETHZ data-sets as lognormal, with average radius 6 μm and a polydispersity of 0.4. The skewness is then $S = 1.264$, which results in a prediction of $\Phi_{RCP} = 0.678$ for the volume fraction of a random close packing of NMC particles. In the particle assemblies created for the 90-,92-,94-,96-% wt. NMC simulations, the observed polydispersities are $\delta = \{0.443, 0.441, 0.438, 0.437\}$ and the skewnesses are $S = \{1.371, 1.353, 1.315, 1.316\}$, respectively, yielding predictions of $\Phi_{RCP} = \{0.686, 0.686, 0.684, 0.684\}$. The volume fraction of the assembly in the DEM simulation is well under this limit when poured (0 bar of compression; see Table 3). After 2000 bar of compression has been applied, the volume fraction exceeds this predicted limit by a small margin, which can be attributed to the particles overlapping in the DEM simulation; while the volume fractions in Table 3 have been measured with the overlapping volumes subtracted so that the volume is counted only once, the existence of overlapping particles can increase the packing fraction beyond the predictions which assume that particles cannot overlap. The volume fraction observed before and after loading is similar to those of experimental random loose packing and random dense packing of steel spheres, as summarized by Brouwers et al. [5].

Parteli et al. [31] uses an approach similar to that of this study to generate a particle assembly by randomly placing particles and then allowing them to settle under gravity. Based on experimental results of gravity-driven packing of fine glass powders, Parteli et al. [31] proposes an empirical relation for the packing fraction as a function of the average particle size $\bar{r}$ (radius): $\Phi = 0.64 - 0.99/(2\bar{r})^{0.676}$. For the assemblies created in the DEM simulation, this yields an estimation of the pre-compacted volume fraction of $\Phi = 0.38$, which well matches that observed. The assembly generated in this study uses no adhesion or Van der Waals forces and still compares favorably to the prediction, while Parteli et al. [31] observes that simulations without these effects may have significantly higher packing fractions.

Table 3
Volume fraction, Φ: observed volume fraction of NMC particles in tomography and DEM particle assembly.

Composition	Pressure	Tomography % vol. NMC	DEM % vol. NMC
90% wt. NMC	0 bar	0.38	0.44
	2000 bar	0.50	0.69
92% wt. NMC	0 bar	0.39	0.51
	2000 bar	0.52	0.69
94% wt. NMC	0 bar	0.44	0.51
	2000 bar	0.54	0.70
96% wt. NMC	0 bar	0.49	0.60
	2000 bar	0.55	0.71

5. Results & discussion

We performed the aforementioned approximations of the imagery and then generated the contact vector lists to find the coordination number and make FTs for each of the ETHZ data-sets.

5.1. Coordination number

The coordination numbers for the data are presented in Table 4. The coordination numbers (z) vary widely between the different contact approximation methods, but the general trend is that the coordination number at 2000 bar (z_{2000}) is higher than that at 0 bar (z_0) indicating that there are more contacts per particle with increasing pressure. The outlier to this trend, the 96% wt. NMC data-set under the voxel contact methods, shows a decrease in z from 0 bar to 2000 bar. While z has decreased with pressure, both the number of particles and contacts have still increased; the number of particles increased more than the number of contacts, an indication of particle splitting.

The coordination numbers in Table 4, derived from the approximations to the tomography and the DEM simulation, are significantly less than the coordination numbers of other random packings of spherical particles, which tend to average 6–8 [43,39,11]. This can be explained by approximation error in the tomographic analysis and weakness of the segmentation algorithm, which may add void space between particles in the process of separating and identifying them. Extra void space between particles would reduce the number of contacts observed in any of the tomography approximations (a)-(e). In the DEM simulation, the coordination numbers average around 2 when unloaded, but

Table 4
Average coordination number, z, at 0 bar and at 2000 bar. Key: (a) Spherical, (b) Ellipsoidal (branch vector), (c) Ellipsoidal (contact normal), (d) Voxel (branch vector), (e) Voxel (contact normal), (f) DEM simulation ($\mu_{k,NMC} = 0.15$), (f′) DEM simulation ($\mu_{k,NMC} = 0$).

z, method	Composition	z_0	z_{2000}	z_{2000}/z_0	$z_{2000}-z_0$
a	90 %wt. NMC	0.510	0.937	1.836	0.427
a	92 %wt. NMC	0.466	1.071	2.298	0.605
a	94 %wt. NMC	0.662	1.062	1.605	0.400
a	96 %wt. NMC	0.939	1.171	1.246	0.231
b, c	90 %wt. NMC	0.321	1.086	3.378	0.764
b, c	92 %wt. NMC	0.331	1.065	3.214	0.733
b, c	94 %wt. NMC	0.422	0.937	2.219	0.515
b, c	96 %wt. NMC	0.656	1.172	1.786	0.516
d, e	90 %wt. NMC	1.294	1.443	1.115	0.149
d, e	92 %wt. NMC	1.261	1.520	1.205	0.259
d, e	94 %wt. NMC	1.452	1.516	1.044	0.065
d, e	96 %wt. NMC	1.605	1.530	0.953	−0.076
f	90 %wt. NMC	1.962	5.404	2.754	3.442
f	92 %wt. NMC	1.913	5.715	2.987	3.801
f	94 %wt. NMC	2.355	6.191	2.629	3.836
f	96 %wt. NMC	2.392	6.389	2.671	3.997
f′	90 %wt. NMC	2.078	5.413	2.605	3.335
f′	92 %wt. NMC	1.333	5.553	4.165	4.220
f′	94 %wt. NMC	2.153	6.116	2.840	3.963
f′	96 %wt. NMC	2.140	6.375	2.979	4.235

exceed 6 after 2000 bar of pressure is applied.

While the DEM simulation gives consistently higher coordination numbers than the imagery-based approximation methods, the trend of increasing z with more pressure holds. The higher z in the DEM simulation itself is not worrisome, as each of the imagery-based approximation methods seems to have its own relative magnitude of z, which may be lower due to the imagery analysis techniques (i.e. watershedding). Further, the ratios of z_{2000}/z_0 for the DEM simulations fall well within the range of the ratios for the tomography-based methods, confirming that the DEM model captures the trend of the coordination number evolving with pressure.

The especially high values of z_{2000} in the DEM simulations can be partially explained by the number of particles; for each electrode composition, the tomography shows an increasing number of particles with increasing pressure, which damps the increase of z with more contacts in approximations (a)–(e). In contrast, each DEM simulation has a constant number of particles for all pressures, so it is to be expected that z_{2000} be significantly higher. Additionally, all of these approximations may understate the contact count by assuming at most one contact between each particle pair.

5.2. Fabric tensor comparison

The FT analysis in this study consists of observing how the contact patterns shift with increasing pressure; therefore, for each data-set and approximation method, the FTs of the 0 bar data and 2000 bar data were compared. Each tensor was statistically tested for fitness by using the χ^2 test described in Appendix B at the 99% significance level. The density differences were computed using the highest-order tensor of significance for the 0 bar and 2000 bar tensors. Thus, if the 0 bar tensor was significant up to the fourth order ($\mathbf{F}_0^{(4)}$) and the 2000 bar tensor was significant up to the second order ($\mathbf{F}_{2000}^{(2)}$), the density difference is reported as $\Delta f^{(4,2)} = f(\mathbf{F}_{2000}^{(2)}) - f(\mathbf{F}_0^{(4)})$. These density differences Δf are plotted as rose diagrams in Fig. 6.

Consider the density difference diagrams in Fig. 6 that represent the spherical, ellipsoidal, and voxel contact approximations: series (a) through (e). While there is some variation in the specific orientation and magnitude of the differences (corresponding to shapes and sizes, respectively of the rose diagrams), the overwhelming trend is that the spatial distribution of contacts decreases in the vertical direction and increases in the lateral direction as pressure increases. This agreement of these five models indicates that very likely, this is the true effect imparted on the cathode assembly by calendaring.

The evolution rose diagrams corresponding to DEM simulation results are presented in Fig. 6, series (f) and (f′). The series (f) simulations were performed with the coefficient of friction between NMC particles $\mu_{NMC} = 0.15$, as listed in Table 2. As an alternative, series (f′) simulations were performed using no friction between NMC particles $\mu_{NMC} = 0$, representing an extremely well-lubricated assembly; this is done to reflect the potentially-lubricative effect of the carbon black and PVDF binder on the friction within the assembly during calendaring.

Fig. 7 shows a zoomed view of the evolution rose diagrams of the DEM simulations presented in Fig. 6, series (f). The magnitude of the density differences is so small compared to those of the tomographic approximations that the color scale for these rose diagrams only varies from a yellow–green/chartreuse to a blue-green/viridian. For the 90–94% wt. NMC evolution diagrams, the DEM results show a positive distribution change in the vertical and lateral directions and a negative distribution change in diagonal directions as pressure increases. The 96% wt. NMC simulation does reproduce the trend of the imagery-based approximations, but the magnitude of this change is extremely small in comparison. Examination of the frictionless series (f′) evolution rose diagrams in Fig. 6 reveals similar results to those of series (f): a very small magnitude of directional density differences and inconsistent rose diagram shape. Therefore, the influence of the friction parameter μ_{NMC} is insufficient to significantly change the character of the evolution of the DEM contact distribution results.

Together, these observations indicate that the contact evolution observed in the DEM simulations (series (f) and (f′)) does not well represent the contact evolution observed in the imagery-based methods (series (a) through (e)). The FT is a critical metric for accurate models of anisotropic phenomena, such as electronic transport through the active particle matrix of an electrode; by failing to capture or reproduce the mechanical directionality, namely the evolution of inter-particle contacts with increasing pressure, using a DEM model of this type has limited utility.

5.3. DEM model critique

Potential flaws in the DEM simulation could be the initial placement of the particles, since the exact particle positions could not be replicated, or that the compression of spherical particles does not correctly capture the trends in the contact distribution. One consideration is that the DEM model employed, though commonly used, does not include interaction forces from adhesion or van der Waals effects which have proven critical to some packing problems [31].

An improvement to increase the accuracy of DEM simulations, which might better preserve the contact distribution, would be to use the multi-sphere method. This method consists of creating an aggregate particle from several overlapping spheres rigidly fixed together. This way, the shape of the particles is better represented, so the contacts of the particles might also be better represented. Several algorithms exist for generating these representations for particles [15]. Since DEM codes are built to consider spherical particles and interactions between spherical particles, the multi-sphere aggregate can be implemented with minimal additional coding and is already implemented in LIGGGHTS [19].

A critical model improvement would be to account for the effect of particle fracture. In the ETHZ data-sets, it is observed that the

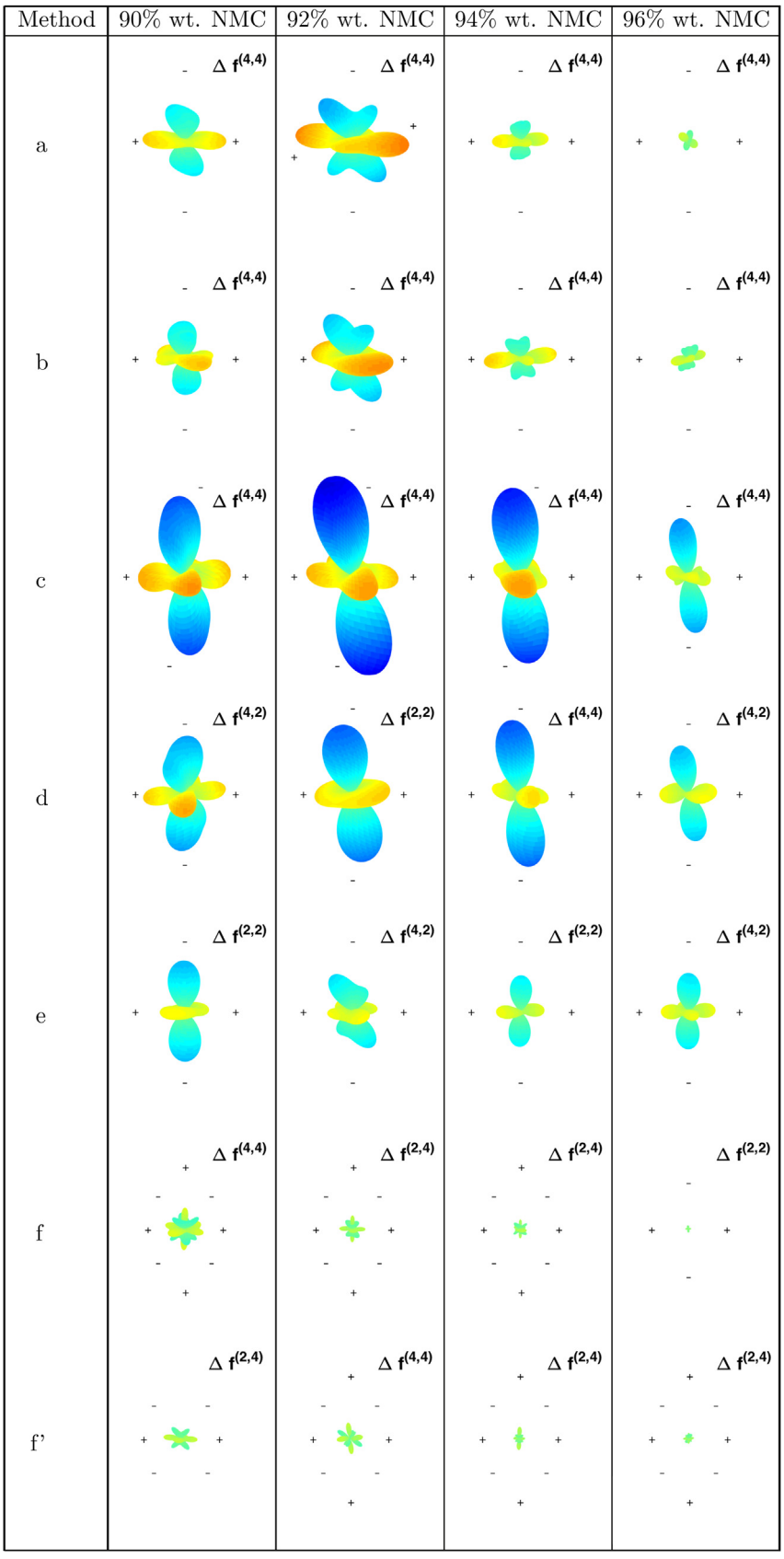

Fig. 6. $\Delta f^{(a,b)} = f(\mathbf{F}_{2000}^{(b)}) - f(\mathbf{F}_{0}^{(a)})$: Fabric tensor evolution rose-diagrams (yellow–orange–red is positive, green-teal-blue is negative); charting evolution of particle contacts from 0 bar to 2000 bar. Fabric tensor order indicated on each plot. Key: (a) Spherical, (b) Ellipsoidal (branch vector), (c) Ellipsoidal (contact normal), (d) Voxel (branch vector), (e) Voxel (contact normal), (f) DEM simulation ($\mu_{NMC} = 0.15$), (f') DEM simulation ($\mu_{NMC} = 0$). (For interpretation of the references to color in this figure legend, the reader is referred to the web version of this article.)

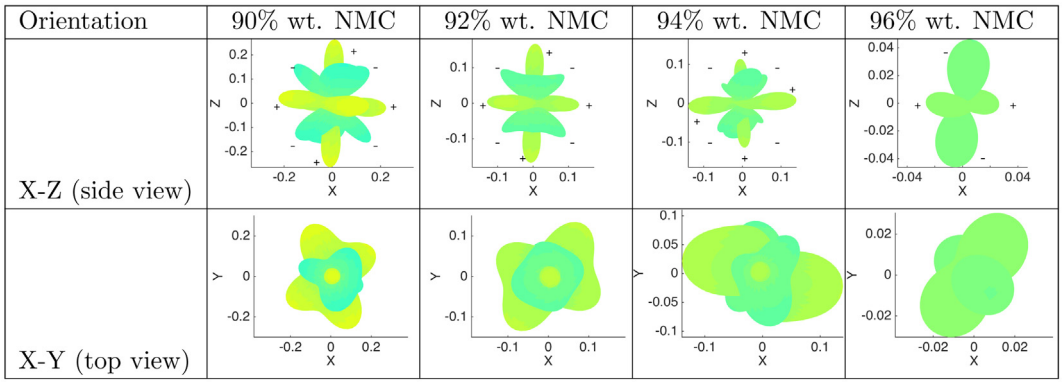

Fig. 7. $\Delta f^{(a,b)} = f(\mathbf{F}_{2000}^{(b)}) - f(\mathbf{F}_{0}^{(a)})$: Close-up of Rose-Diagrams of DEM simulation (f: $\mu_{k,NMC} = 0.15$) (yellow–orange–red is positive, green-teal-blue is negative). In this case, the magnitude of the density differences is so small that the color scale for these rose diagrams only varies from a yellow–green/chartreuse (positive) to a blue-green/viridian (negative). Note: scale varies per image to provide zoomed view. (For interpretation of the references to color in this figure legend, the reader is referred to the web version of this article.)

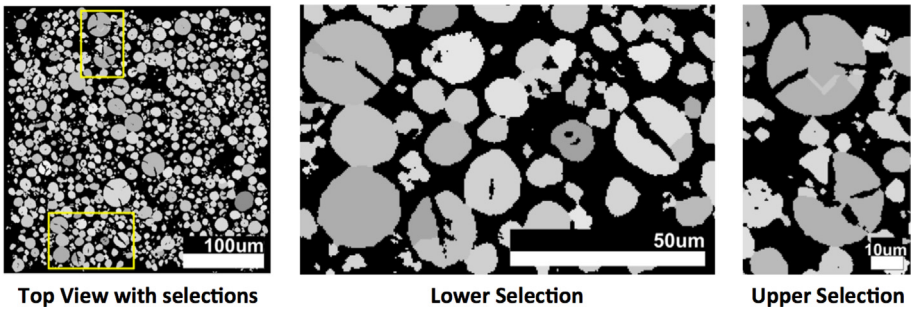

Fig. 8. 92% wt. NMC, 2000 bar data-set, particle assembly illustrating particle fracture: (left) slice showing top view, each particle given a unique greyscale color for identification, and two selection for zoom; (center) lower selection, (right) upper selection. (For interpretation of the references to color in this figure legend, the reader is referred to the web version of this article.)

mean fragment size decreases and sphericity (a measure of how round the particle is) decreases as pressure increases – indications that particle fracture is prevalent; this can be confirmed by visual examination of the tomography [13] (see Fig. 8). Experimental studies have found that crushing a material requires more energy as the particle size decreases [4] and have confirmed that larger particles are more likely to break than smaller particles under the same load [36]. Larger particles, which tend to have more particle contacts, may be more likely to fracture because a larger portion of the particle will be in the vicinity of a contact point, and therefore have a critical stress that might cause cracks to initiate from surface flaws [36]. The tendency of larger particles to be more likely to fracture is evident in the NMC tomography.

Leaving the particle to be represented as a sphere in DEM models, a particle could be split into two or more pieces once a splitting stress criterion is met [24,26]. A particle size distribution could be estimated and applied to generate fragments [36]. Alternatively, one could model the initial particles using the multi-sphere method and break the grouping into two or more once splitting occurs [15]. A drawback to these solutions is a trade-off between conserving mass and having spatially disparate fragments [26,36]. If the particle to be split is replaced with a series of particles that are spatially disparate, as proposed by Lobo-Guerrero et al. [24], then the mass of the particle is not conserved without adjustments to particle density or particle locations and kinematics [36]. In contrast, if the particles are split into fragments which conserve mass but overlap, as proposed by McDowell et al. [26], then artificial interaction forces, essentially a false 'fissile' energy, are induced [36].

6. Conclusions

We have explored the use of the fabric tensor as a method of modeling the inter-particle contacts and connectivity of the active particle network in the battery electrode microstructure. This approach yields the understanding that inter-particle contacts become increasingly lateral in proportion as the pressure increases on the matrix. Inter-particle contacts represent the electrical conductivity through the porous electrode matrix for efficient capacity retention and rate performance. Drawing from the areas of granular media and damage mechanics, the fabric tensor analysis may offer a formulation to represent the deformation, deterioration, and performance of the electrodes at the macroscale.

The application of the fabric tensor to model the evolution of inter-particle contacts with increasing pressure results in the realization that the common discrete element method model for this problem falls short. When evaluating the DEM results for directional quantities, such as the inter-particle contacts, the fabric tensor analysis reveals that the DEM model does not accurately reproduce the behavior observed in the tomography. More accurate methods for particle shape representation and the models for interaction between the particles may be warranted.

This current article describes the effect of calendaring pressure on the electrode microstructure and mechanical deformation of the cathode particles using fabric tensors, but this analysis can be extended in several ways to further enhance the understanding of battery electrode microstructural mechanics. One augmentation could be to account for the contact size between two particles, rather than simply its existence, which would provide a better

representation of the inter-particle contact network. Additionally, further examination of the interstitial void space would yield better understanding of the Li^+ ionic transport in the porous electrode matrix during battery charging and discharging. Analysis of the evolution of the fabric tensors can be used to build corresponding damage tensors to represent the particle assembly in continuum mechanical models [25,47] and can be either validated or supported by experimental methods such as X-ray tomography and other imaging methods [28,14,49]. Such extensions will explored in our future work.

Acknowledgments

Work performed contributing to the underlying research and publication was supported by Andrew Stershic's Department of Energy Computational Science Graduate Fellowship, under grant DE-FG02-97ER25308. Dr. Nanda acknowledges support from the Vehicle Technologies Program, under Energy Efficiency and Renewable Energy (EERE) Office of the Department of Energy.

The submitted manuscript has been authored by a contractor of the U.S. Government under Contract No. DE-AC05-00OR22725. Accordingly, the U.S. Government retains a non-exclusive, royalty-free license to publish or reproduce the published form of this contribution, or allow others to do so, for U.S. Government purposes.

The authors would like to acknowledge the Laboratory of Nanoelectronics at ETHZ for their openness in providing their dataset for public use. The authors would like to thank Oak Ridge National Laboratory for hosting Mr. Stershic for his fellowship practicum in 2013.

A. Particle approximation for contact analysis

A.1. Spherical approximation

This method consists of approximating each particle by a sphere and then generating a list of contact vectors by observing spheres that overlap. The approximation of the particles as spheres is common; Ebner et al. [13] describes the NMC particles as spheres qualitatively and quantitatively, using the normalized lengths of the long and short axes to classify the NMC particles as equant (nearly spherical) ellipsoids [12]; inspection of the tomography confirms their generally-spherical shape. In this scheme, overlap of the spheres is a proxy for contact as those particles in deformed adjacency due to contact in reality would likely show as overlapping in this simple method. The spheres are generated using the centroid and volume of each particle from the tabulated particle information. In this way, the location and volume of the particles are preserved, but any deviation from a spherical shape (eccentricity, orientation) is not. Contact can be found by comparing the distance between the centroids of two spheres to the sum of their radii.

A.2. Ellipsoidal approximation

While the particles in these domains can be described qualitatively as spherical, the particles deform in response to applied loads and the matrix around them. Thus, an ellipsoidal approximation may better approximate the geometry of the set of particles, and thus provide better insight into the inter-particle contacts.

In this scheme, overlap of the ellipsoids is a proxy for contact as those particles in deformed adjacency due to contact in reality, as before. Our strategy for generating an ellipsoid from the given data was to first isolate each particle in the tomography and create a list of voxels comprising that particle. From this list, a polygonal surface triangulation is generated using the powercrust algorithm [1,2]. The mesh is reduced to a computationally-efficient size using a mesh simplification algorithm [16]. The remaining nodes of the mesh are then approximated by an arbitrary three-dimensional ellipsoid using a least squares fit [34]. Since this approximation fits the surface of the ellipsoid without preserving the volume, the volume of the proposed approximation is then examined. If the proposed volume deviates significantly from the true volume, then a spherical approximation is used. This eliminates the generation of highly-elongated ellipsoids that are not found in the tomography.

Contact between ellipsoids is determined using a method created for determining ellipsoid contacts for DEM simulations introduced by Perram & Wertheim [33] and adapted by Donev et al. [10]. The process is to volumetrically expand or contract each pair of ellipsoids under consideration by a scalar factor μ until the two are just tangent. If $\mu > 1$, there is no contact, as the ellipsoids would need to be expanded in order to reach tangency. Likewise, $\mu \leq 1$ indicates contact as the ellipsoids would need to be shrinked in order to reach tangency [32,10].

Pairs of contacting particles can be found using this algorithm on all pairs of ellipsoids within the domain. The centroidal vector (branch vector) and contact patch normals are used to build fabric tensors using this approximation (see illustration in Fig. 1). The centroidal contact vector involves calculating the branch vector between the centroids of contacting particles [37]. This method is free of approximation error of the contact algorithm, but loses the exact direction of the contact normal. This approximation works exactly for spherical particles, but as the particles become increasingly eccentric, the branch vector may deviate further from the contact normal. In contrast, using the contact normal vector generated by the contact algorithm may increase the approximation accuracy by characterizing the actual contact direction, but it relies entirely on the accuracy of the contact algorithm.

A.3. Voxel-based method

This method involves directly using the imagery generated by the SRXTM process to see if any pairs of particles are abutting, with the assumption that two particles directly adjacent to one another are in contact. The ETHZ group modified the raw imagery with the particle identification analysis to uniquely color each particle. For each voxel in the set, 13 adjacent voxels (half of the 26 possible to prevent double-checking a given voxel pair) are checked to see if the color (proxy for particle number) is the same as its own. If the color is different and does not correspond to the color of the background matrix, then the two particles are said to be in contact. It should be noted that during particle identification, the water-shedding process tends to shrink particles as it separates particles by adding a minimal zone of void material between identified particles. This may decrease the occurrence of adjacent voxels of different particles, making this calculation less accurate.

As with the ellipsoidal approximation method, there are two ways to generate a list of contact vectors: centroidal and contact-based. In the centroidal method, when any two contacts are said to be in contact, the branch vector between the two particles' centroids is saved. This method is the simplest and while the vector calculated may not be the closest approximation to the actual contact normal, it is free of approximation error. The alternative is to use the contacting surfaces to generate the normal vector. For this method, the contact vector is the average of all the vectors between all adjacent voxels of a given pair of particles.

B. Statistical significance

Kanatani outlined tests for statistical significance of fitness of

the distribution based on the "test of uniformity" [18]. This tests the hypothesis that the distribution $f(\vec{n})$ matches the lower-rank approximation (starting with the uniform/isotropic value of $1/4\pi$) against the null hypothesis that non-zero terms are statistical variations due to the sample size. The solution is to calculate a likelihood ratio, which if high, indicates that the distribution likely matches the lower-rank distribution and that higher-rank tensors are negligible, and if low, indicates that the distribution likely does not match and that the higher-rank tensors are significant [18]. The tensors of the third kind (**D**) are particularly useful for this, as they isolate the effect of going to each higher rank. Kanatani gives the following statistic (λ) to be tested against a χ^2_c distribution. For second rank: $\lambda = \frac{2N}{15} D^{(2)}_{ij} D^{(2)}_{kl}$ is tested against $\chi^2_c(5,\alpha)$, where α is the significance level. For fourth rank: $\lambda = \frac{8N}{315}\left(D^{(4)}_{ijkl}D^{(4)}_{ijkl} - \frac{8}{11}D^{(4)}_{ijkl}D^{(4)}_{ijkm}D^{(2)}_{lm}\right)$ is tested against $\chi^2_c(9,\alpha)$ [18]. As the statistic of significance is given up to the fourth rank, we use the highest-rank approximation of statistical significance up to the fourth rank in this analysis.

References

[1] N. Amenta, S. Choi, R.K. Kolluri, The power crust, unions of balls, and the medial axis transform, Comput. Geom. Theory Appl. 19 (2000) 127–153.
[2] N. Amenta, S. Choi, R.K. Kolluri, The power crust, in: 6th ACM Symposium on Solid Modeling Proceedings, 2001, pp. 249–260. http://www.cs.ucdavis.edu/amenta/powercrust.html.
[3] M. Armand, J.-M. Tarascon, Building better batteries, Nature 451 (7179) (2008) 652–657.
[4] Y. Bar-Cohen, K. Zacny, Drilling in Extreme Environments: Penetration and Sampling on Earth and Other Planets, John Wiley & Sons, 2009.
[5] H. Brouwers, Particle-size distribution and packing fraction of geometric random packings, Phys. Rev. E 74 (3) (2006) 031309.
[6] D.-W. Chung, M. Ebner, D.R. Ely, V. Wood, R.E. García, Validity of the Bruggeman relation for porous electrodes, Model. Simul. Mater. Sci. Eng. 21 (7) (2013) 074009.
[7] D.-W. Chung, P.R. Shearing, N.P. Brandon, S.J. Harris, R.E. García, Particle size polydispersity in Li-ion batteries, J. Electrochem. Soc. 161 (3) (2014) A422–A430.
[8] P.A. Cundall, O.D. Strack, A discrete numerical model for granular assemblies, Géotechnique 29 (1) (1979) 47–65.
[9] K.W. Desmond, E.R. Weeks, Influence of particle size distribution on random close packing of spheres, Phys. Rev. E 90 (2) (2014) 022204.
[10] A. Donev, S. Torquato, F.H. Stillinger, Neighbor list collision-driven molecular dynamics simulation for nonspherical hard particles.: II. applications to ellipses and ellipsoids, J. Comput. Phys. 202 (2) (2005) 765–793.
[11] X. Dou, Y. Mao, Y. Zhang, Effects of contact force model and size distribution on microsized granular packing, J. Manuf. Sci. Eng. 136 (2) (1966) 89–90.
[12] M. Ebner, D.-W. Chung, R.E. García, V. Wood, Tortuosity anisotropy in lithium-ion battery electrodes, Adv. Energy Mater. 4 (5) (2014), http://dx.doi.org/10.1002/aenm.201301278.
[13] M. Ebner, F. Geldmacher, F. Marone, M. Stampanoni, V. Wood, X-ray tomography of porous, transition metal oxide based lithium ion battery electrodes, Adv. Energy Mater. 3 (2013) 845–850.
[14] M. Ebner, F. Marone, M. Stampanoni, V. Wood, Visualization and quantification of electrochemical and mechanical degradation in Li ion batteries, Science 342 (6159) (2013) 716–720.
[15] J.-F. Ferellec, G.R. McDowell, A method to model realistic particle shape and inertia in DEM, Granul. Matter 12 (5) (2010) 459–467.
[16] M. Garland, Quadric-based Polygonal Surface Simplification, Ph.D. thesis, Georgia Institute of Technology, 1999, http://www.cs.cmu.edu/afs/cs/Web/People/garland/quadrics/qslim.html.
[17] C. Glaize, S. Genies, Lithium Batteries and Other Electrochemical Storage Systems, John Wiley & Sons, 2013.
[18] K.-I. Kanatani, Distribution of directional data and fabric tensors, Int. J. Eng. Sci. 22 (2) (1984) 149–164.
[19] C. Kloss, C. Goniva, A. Hager, S. Amberger, S. Pirker, Models, algorithms and validation for opensource DEM and CFD–DEM, Prog. Comput. Fluid Dyn. Int. J. 12 (2) (2012) 140–152. http://www.cfdem.com.
[20] D. Kolymbas, Constitutive Modelling of Granular Materials, Springer Science & Business Media, 2000.
[21] Laboratory for Nanoelectronics, ETH Zürich, X-ray Tomography, URL: http://data-archive.ethz.ch/delivery/action/collectionViewer.do?operation=viewCollection&displayType=List&collectionId=2735301.
[22] D. Larcher, J. Tarascon, Towards greener and more sustainable batteries for electrical energy storage, Nat. Chem..
[23] Z. Liu, J.S. Cronin, K. Yu-chen, J.R. Wilson, K.J. Yakal-Kremski, J. Wang, K.T. Faber, S.A. Barnett, Three-dimensional morphological measurements of $LiCoO_2$ and $LiCoO_2$/Li($Ni_{1/3}$ $Mn_{1/3}$ $Co_{1/3}$)O_2 lithium-ion battery cathodes, J. Power Sources 227 (2013) 267–274.
[24] S. Lobo-Guerrero, L.E. Vallejo, Crushing a weak granular material: experimental numerical analyses, Géotechnique 55 (4) (2005) 245–249. http://www.icevirtuallibrary.com/content/article/10.1680/geot.2005.55.3.245.
[25] V. Lubarda, D. Krajcinovic, Damage tensors and the crack density distribution, Int. J. Solids Struct. 30 (20) (1993) 2859–2877.
[26] G. R. McDowell, J. P. de Bono, On the micro mechanics of one-dimensional normal compression, Géotechnique 63.
[27] M. Moesen, MMTensor 1.0, 2011. http://www.mathworks.com/matlabcentral/fileexchange/32891-mmtensor-1-0.
[28] J. Nanda, H. Bilheux, S. Voisin, G.M. Veith, R. Archibald, L. Walker, S. Allu, N.J. Dudney, S. Pannala, Anomalous discharge product distribution in lithium-air cathodes, J. Phys. Chem. C 116 (15) (2012) 8401–8408.
[29] P.K.V.V. Nukala, S. Simunovic, An efficient algorithm for simulating fracture using large fuse networks, J. Phys. A Math. Gen. 36 (45) (2003) 11403.
[30] J.-K. Park, Principles and Applications of Lithium Secondary Batteries, John Wiley & Sons, 2012.
[31] E. J. Parteli, J. Schmidt, C. Blümel, K.-E. Wirth, W. Peukert, T. Pöschel, Attractive particle interaction forces and packing density of fine glass powders, Sci. Rep. 4.
[32] J.W. Perram, J. Rasmussen, E. Præstgaard, J.L. Lebowitz, Ellipsoid contact potential: theory and relation to overlap potentials, Phys. Rev. E 54 (1996) 6565–6572. http://link.aps.org/doi/10.1103/PhysRevE.54.6565.
[33] J.W. Perram, M. Wertheim, Statistical mechanics of hard ellipsoids. I. Overlap algorithm and the contact function, J. Comput. Phys. 58 (3) (1985) 409–416.
[34] Y. Petrov, Ellipsoid Fit, 2009. http://www.mathworks.com/matlabcentral/fileexchange/24693-ellipsoid-fit.
[35] S. Plimpton, Fast parallel algorithms for short-range molecular dynamics, J. Comput. Phys. 117 (1) (1995) 1–19. http://lammps.sandia.gov.
[36] T. Pöschel, T. Schwager, Computational Granular Dynamics: models and Algorithms, Springer Science & Business Media, 2005.
[37] F. Radjaï, J. Lanier, Experimental and numerical analysis of local variables in granlar materials, in: B. Cambou, M. Jean, F. Radjaï, et al. (Eds.), Micromechanics of Granular Materials, Wiley Online Library, 2009, pp. 1–45.
[38] J. Rahmoun, D. Kondo, O. Millet, A 3D fourth order fabric tensor approach of anisotropy in granular media, Comput. Mater. Sci. 46 (4) (2009) 869–880.
[39] A.D. Rosato, O. Dybenko, D.J. Horntrop, V. Ratnaswamy, L. Kondic, Microstructure evolution in density relaxation by tapping, Phys. Rev. E 81 (6) (2010) 061301.
[40] M. Saadatfar, A.P. Sheppard, T.J. Senden, A.J. Kabla, Mapping forces in a 3d elastic assembly of grains, J. Mech. Phys. Solids 60 (1) (2012) 55–66.
[41] M. Satake, Fabric tensor in granular materials, in: Proc., IUTAM Symp. On Deformation and Failure of Granular Materials, Delft, The Netherlands, 1982, pp. 63–68.
[42] Y. Sheng, C.R. Fell, Y.K. Son, B.M. Metz, J. Jiang, B.C. Church, Effect of calendering on electrode wettability in lithium-ion batteries, Front. Energy Res. 2 (2014) 56.
[43] Y. Shi, Y. Zhang, Simulation of random packing of spherical particles with different size distributions, in: ASME 2006 International Mechanical Engineering Congress and Exposition, American Society of Mechanical Engineers, 2006, pp. 539–544.
[44] M. Smith, R.E. García, Q.C. Horn, The effect of microstructure on the galvanostatic discharge of graphite anode electrodes in $LiCoO_2$-based rocking-chair rechargeable batteries, J. Electrochem. Soc. 156 (11) (2009) A896–A904.
[45] G. Subhash, S. Nemat-Nasser, M. Mehrabadi, H. Shodj, Experimental investigation of fabric-stress relations in granular materials, Mech. Mater. 11 (2) (1991) 87–106.
[46] A. Thaler, D. Watzenig, Automotive Battery Technology, Springer, 2014.
[47] G.Z. Voyiadjis, P.I. Kattan, Damage mechanics with fabric tensors, Mech. Adv. Mater. Struct. 13 (4) (2006) 285–301.
[48] B. Yan, C. Lim, L. Yin, L. Zhu, Three dimensional simulation of galvanostatic discharge of $LiCoO_2$ cathode based on x-ray nano-ct images, J. Electrochem. Soc. 159 (10) (2012) A1604–A1614.
[49] F. Yang, Y. Liu, S.K. Martha, Z. Wu, J.C. Andrews, G.E. Ice, P. Pianetta, J. Nanda, Nanoscale morphological and chemical changes of high voltage lithium–manganese rich nmc composite cathodes with cycling, Nano Lett. 14 (8) (2014) 4334–4341.
[50] L. Yi, K. Dong, R. Zou, A. Yu, Coordination number of the packing of ternary mixtures of spheres: DEM simulations versus measurements, Ind. Eng. Chem. Res. 50 (14) (2011) 8773–8785.
[51] M. Yoshio, R.J. Brodd, A. Kozawa, Lithium-ion Batteries, vol. 1, Springer, 2009.
[52] H. Zheng, R. Yang, G. Liu, X. Song, V.S. Battaglia, Cooperation between active material, polymeric binder and conductive carbon additive in lithium ion battery cathode, J. Phys. Chem. C 116 (7) (2012) 4875–4882.